

Microstructure-based cleavage modelling to study grain size refinement and simulated heat affected zones of S690 high strength steel

Jiang, Quanxin; Bertolo, Virginia M.; Popovich, Vera; Sietsma, Jilt; Walters, Carey L.

DOI

[10.1016/j.msea.2023.145184](https://doi.org/10.1016/j.msea.2023.145184)

Publication date

2023

Document Version

Final published version

Published in

Materials Science and Engineering A

Citation (APA)

Jiang, Q., Bertolo, V. M., Popovich, V., Sietsma, J., & Walters, C. L. (2023). Microstructure-based cleavage modelling to study grain size refinement and simulated heat affected zones of S690 high strength steel. *Materials Science and Engineering A*, 876, Article 145184. <https://doi.org/10.1016/j.msea.2023.145184>

Important note

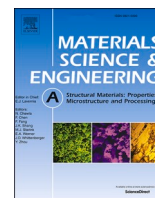
To cite this publication, please use the final published version (if applicable).
Please check the document version above.

Copyright

Other than for strictly personal use, it is not permitted to download, forward or distribute the text or part of it, without the consent of the author(s) and/or copyright holder(s), unless the work is under an open content license such as Creative Commons.

Takedown policy

Please contact us and provide details if you believe this document breaches copyrights.
We will remove access to the work immediately and investigate your claim.



Microstructure-based cleavage modelling to study grain size refinement and simulated heat affected zones of S690 high strength steel

Quanxin Jiang^{a,*}, Virgínia M. Bertolo^a, Vera Popovich^a, Jilt Sietsma^a, Carey L. Walters^b

^a Materials Science and Engineering, Delft University of Technology, Delft, the Netherlands

^b Maritime and Transport Technology, Delft University of Technology, Delft, the Netherlands

ARTICLE INFO

Keywords:

Cleavage
Multi-barrier modelling
Local approach to fracture
Grain refinement
HAZ

ABSTRACT

Study of the cleavage behavior of heat treated S690 steel by a microstructure-based approach combined with finite element analysis is present in this paper. Cleavage simulations of steels subjected to heat treatments that cause grain refinement or simulate heat affected zones are performed, and are compared with experiments. It is found that the experimental improvement of toughness from grain refinement is 80% of what would be expected based on the model. The 20% difference is due to the lower number fraction of high-angle misorientation boundaries. It is also found that the resistance to micro-crack propagation is more effective in heat affected zones, which can be explained by the residual compressive stress in martensite-austenite constituents. This research assesses the balance between microstructural parameters for controlling cleavage toughness.

1. Introduction

Processing parameters (e.g. weld travel speed, process, wire composition, cooling rate, etc.) determine the ability of the microstructure of high strength steel to generate sufficiently tough base metal/weld/Heat Affected Zone (HAZ) combination [1]. It is essential to know the separate and combined effects of various microstructural features on cleavage, such as prior austenite grain size [2], carbide size [3], the presence of inclusions [4], M-A (martensite-austenite) phases [5], precipitates, etc. (for an overview, see Ref. [6]). Better modelling of the relationship between the microstructures resulting from welding processes and HAZ toughness can lead to more cost effective development and usage of welding procedures.

Austenite grain refinement has been recognized as an effective method to improve mechanical properties of high strength steels [7–9]. There are multiple studies performed on refining of austenite grain size [10–14]. However, high strength steels often have bainitic or martensitic microstructure, which has hierarchical crystallographic structures. In this case, the definition of grain is complicated, as a grain can be defined as prior austenite grain (PAG), packet, block, or lath [15]. Although it is generally observed that the refinement of a prior austenite grain can improve both strength and toughness of steel, it is also reported that the PAG refinement is less effective than expected as the local fracture stress is observed with little influence [16]. A modelling

method that can incorporate comprehensive microstructure is needed to help estimate the effectiveness of grain refinement. There are a few attempts [17,18] to model the effect of grain size on cleavage toughness of steels using microstructure-based methods. However, those attempts did not validate the effect of isoparametric change in grain size.

Welding thermal cycles produce heterogeneous microstructure in the HAZ [19]. Coarse-grained heat affected zone (CGHAZ) and intercritically reheated coarse-grained heat affected zone (ICCGHAZ) are found to have low fracture toughness due to the coarsening of austenite grains and the formation of martensite-austenite (M-A) constituents [20–23]. One of the complexities of modelling the fracture process in an HAZ is when there are pre-existing carbides and brittle inclusions in the base material. Li and Baker [24] observed in a V and Nb microalloyed steel that M-A constituents have a more pronounced impact on the fracture process of ICCGHAZ than pre-existing carbides and aluminium oxide inclusions. Vassilaros [25] found in ultra-low carbon bainitic steel that the pre-existing TiN inclusions rather than M-A constituents trigger cleavage fracture in the CGHAZ. Therefore, a modelling method that can consider different types of brittle particles is needed to better understand the cleavage micromechanisms in a welded multi-phase steel.

This study contributes new knowledge to the understanding of cleavage fracture of steels subjected to heat treatments that cause grain refinement or simulate heat affected zones. The first objective is to estimate the effect of grain refinement on toughness improvement of a

* Corresponding author. Mekelweg 2, 2628 CD, Delft, the Netherlands.

E-mail address: q.jiang-1@tudelft.nl (Q. Jiang).

<https://doi.org/10.1016/j.msea.2023.145184>

Received 12 January 2023; Received in revised form 16 May 2023; Accepted 16 May 2023

Available online 18 May 2023

0921-5093/© 2023 The Authors. Published by Elsevier B.V. This is an open access article under the CC BY license (<http://creativecommons.org/licenses/by/4.0/>).

multi-phase steel, with numerical simulations and validation from a mostly isoparametric experimental program. It investigates how model parameters should be adjusted for changes in prior austenite grain substructures. The second objective is to simulate the cleavage fracture in welded steels with different types of brittle particles. It provides insight into the modelling of toughness degradation in CGHAZ and ICCGHAZ that contain pre-existing brittle inclusions.

The numerical method used in this paper was proposed by Jiang et al. [26]. Several microstructural features (grain size, hard particle size, and hard particle geometries) are considered simultaneously, and the deactivation of crack initiators is incrementally considered. This approach is based on prior multi-barrier models [27,28]. Cleavage parameters K_{Ia}^{mm} (crack arrest of the grain boundary), and σ_H^c (critical fracture stress of hard inclusion) are the values fitted from fracture experiments and can be used to estimate the effect of microstructures affected heat treatments.

The current research applies the method to model the cleavage behavior of Gleeble heat treated S690 QT steel at $-100\text{ }^\circ\text{C}$ and $-40\text{ }^\circ\text{C}$. The first type of heat treatment is a rapid cyclic heating (RCH) to represent variation of microstructure that solely refines the grains. The second type of heat treatment simulates HAZs, which represents welded microstructures where grains are coarsened and martensite-austenite (M-A) constituents are generated. In addition, theoretical calculation based on a multi-barrier model [26] are performed for variations of microstructural parameters, such as grain size and hard particle distributions (while keeping other modelling parameters constrained). The heat-treated materials' fracture behaviours are compared with the theoretical calculations.

2. Materials

A commercially available 80 mm thick quenched and tempered S690 high strength steel plate is used in this paper. The chosen thickness position for this study is the middle section that represents the worst fracture toughness of the S690 QT steel plate. The chemical composition of the as-received steel was studied by XRF (X-ray fluorescence) and LECO combustion analysis [34]. The chemical composition is shown in Table 1.

Gleeble heat treatments were carried out to generate a grain refined microstructure, coarse-grained heat affected zone (CGHAZ) and intercritically reheated coarse-grained heat affected zone (ICCGHAZ). The details of the heat treatment can be found in Refs. [29,30] and a brief description is provided in the following paragraphs.

The RCH treatment route is applied to generate a refined grain microstructure, which includes the following steps: heating up the sample from room temperature to $870\text{ }^\circ\text{C}$ (above A_{c3}) at $20\text{ }^\circ\text{C/s}$ and soaking at $870\text{ }^\circ\text{C}$ for 120 s; afterwards, industrial quenching and tempering heating and cooling profiles are used in to keep the microstructure and composition as close as possible to the as-received steel.

The thermal profile for the CGHAZ was experimentally obtained from an actual gas metal arc welding with a heat input of 2.2 kJ/mm . For the ICCGHAZ, the thermal profile for the first cycle was the same as used for the CGHAZ, followed by a second cycle with the same heating and cooling rates as the first step, but with peak temperature $750\text{ }^\circ\text{C}$ (within the critical A_{c1} and A_{c3} temperatures).

The fracture tests were performed at $-100\text{ }^\circ\text{C}$ for the RCH treated steel, and at $-40\text{ }^\circ\text{C}$ for CGHAZ and ICCGHAZ. Fracture tests of the as-received reference steel were performed at both $-100\text{ }^\circ\text{C}$ and $-40\text{ }^\circ\text{C}$. The different test temperature is aimed to have fracture mode of heat

Table 1
Chemical composition of S690 QT [34].

Composition	Fe	C	Si	Al	Mo	Other
wt (%)	Bal.	0.160 ± 0.001	0.30 ± 0.03	0.08 ± 0.01	0.29 ± 0.02	Mn, Ni, Cr, Nb

treated steels in cleavage.

2.1. Microstructures

The as-received material has a microstructure of 64% tempered bainite, 29% tempered martensite, and of less than 7% ferrite [29]. The RCH treatment was designed to keep the microstructure of the as-received steel and the phases observed in the as-received steel remained present as shown in Fig. 1. The specimens of CGHAZ contain 88% auto-tempered martensite, 6% martensite and 6% coalesced martensite. The specimens of ICCGHAZ have a microstructure of 71% granular bainite, 12% auto-tempered martensite, 8% martensite, and of less than 10% ferrite [30]. Fig. 1 shows the overview of microstructures of the steels. Details of the microstructure characterization can be found in Refs. [29,31].

Prior Austenite Grains (PAG) are reconstructed based on EBSD measurements [29,30]. The EBSD measurements were repeated at different locations for each steel. The statistical distribution of the grain size (D in μm) is obtained by least-square fitting of the grain size data to the function $P(D)$. $P(D)$ represents the probability that a grain size is larger than D μm , and is a combined function of lognormal distribution and power-law distribution:

$$P(D) = \min \left\{ 1 - CDF(D, \mu, S), \frac{\alpha}{D^\beta} \right\} \quad (1)$$

with $CDF(D, \mu, S)$ is the cumulative distribution function of a lognormal distribution, representing $1/2 + 1/2 \operatorname{erf} \left(\frac{\ln D - \mu}{\sqrt{2} S} \right)$, where α and β are fitting parameters, μ is the mean and S is the standard deviation.

Fig. 2 shows the grain size data measured from EBSD with the fitted curves for the as-received steel, RCH treated steel, CGHAZ, and ICCGHAZ. After the RCH treatment, grain refinement by 55% (in terms of average value) was achieved. After the HAZ heat treatment, grains are coarsened by 195% and 237% (in terms of average value), for CGHAZ and ICCGHAZ, respectively. The cusp in the plot is explained by the change between the two fitted probability functions. It is observed in Fig. 2 that when eq. (1) shift from lognormal distribution to power law distribution the cusp is concave. It indicates a nonproportional change in the tail of the grain size distribution compared with the mean. For RCH and HAZ treatments, the large-grain tail of the distribution becomes thinner compared to the as-received material.

The hard particles that act as initiator of cleavage cracks in the as-received steel and in the steel after grain refinement are found to be circular oxides that are in the size range of $1\text{--}5\text{ }\mu\text{m}$ and rectangular Nb-rich inclusions that are in the size range of $1\text{--}12\text{ }\mu\text{m}$. The oxides and Nb-rich inclusions are not changed after the heat treatments, and the characterization performed in as-received steel is used to model the particle distributions in the heat-treated steels. The size of circular inclusions (oxides) is measured as equivalent diameter, while the rectangular inclusions (Nb-rich inclusions) are represented by the longer axis. Fig. 3 shows the inclusion size distributions measured by Keyence digital microscope. The number density of oxides and Nb inclusions is calculated as 38 and 13 per 0.001 mm^3 , respectively, which is converted from 2D measurements according to Schwartz-Saltykov method [31]. In the CGHAZ and ICCGHAZ, M-A constituents in sizes of less than $1\text{ }\mu\text{m}$ are present. The longer axis of M-A constituents are measured, and the size distribution is shown in Fig. 4. The M-A constituents are distributed with a density of 7.2×10^5 and 1.38×10^6 per 0.001 mm^3 for CGHAZ and ICCGHAZ, respectively. Eq. (1) is used to fit the statistical distribution of hard particles, which provides input for the cleavage modelling.

2.2. Tensile properties

Tensile tests were carried out at room temperature using cylindrical specimens. The tensile specimens for as-received material have a gauge length of 60 mm with a gauge diameter of 8 mm and were tested at a

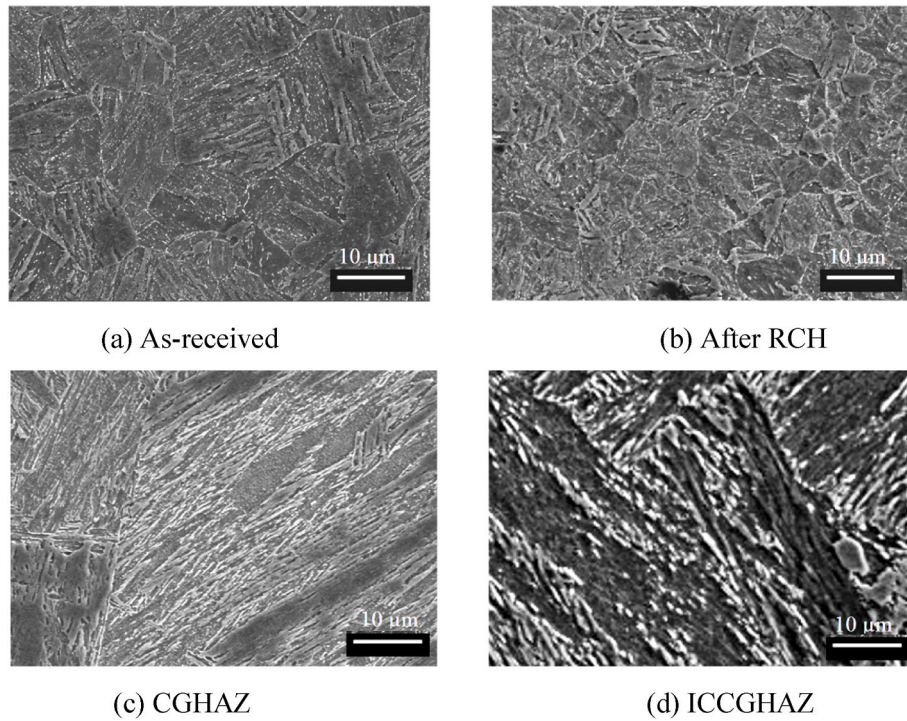


Fig. 1. Micrographs of S690QT steel before (a) and after heat treatments (b)–(d) [29,30].

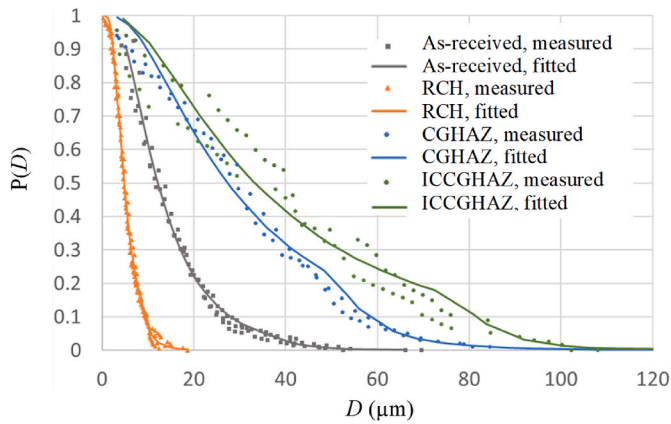


Fig. 2. Distribution of the major axis of PAG.

deformation rate of 1.2 mm/s in order to apply similar strain rate conditions as in CTOD specimens. The tensile specimens for heat-treated material have a gauge length of 10 mm with a gauge diameter of 5.65 mm and were accordingly tested at a deformation rate of 0.2 mm/s. The stress-strain relationship of the steels is characterized by Ludwik's law, which is defined with the flow stress (σ) and the effective plastic strain (ϵ_p) as:

$$\sigma = \sigma_y + K \epsilon_p^{n_L} \quad (2)$$

where, σ_y , K and n_L are material parameters. The parameters of Ludwik's law are fitted from tensile tests at room temperature and are converted to tensile curves at the fracture temperatures (according to ISO 12135 [32]) to generate material input for FE models.

$$\sigma_{low\ temperature} = \sigma_{room\ temperature} + \frac{10^5}{(491 + 1.8T)} - 189 \quad (3)$$

where T is the low temperature in °C. Fig. 5 shows the comparison of

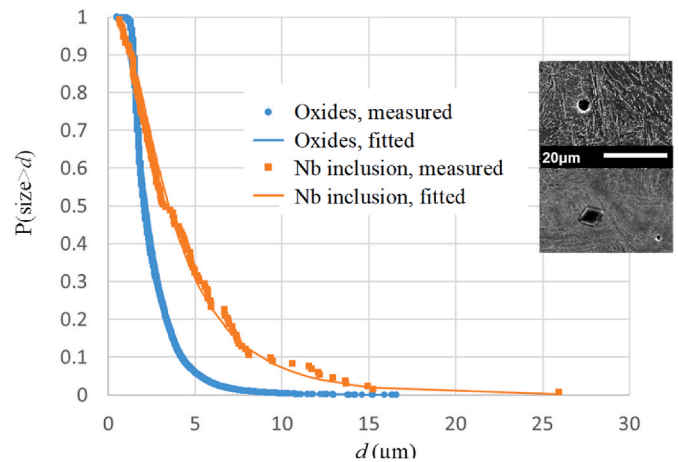


Fig. 3. Size distribution of inclusions (with SEM micrographs showing the morphology).

flow stress versus plastic strain relationships fitted for the steels and converted to the fracture temperatures. Table 2 shows the summary of tensile test results.

As the hardening behavior shows differences among the steels, the representative flow stress for comparison is defined by the average of yield strength (0.2%-offset stress) and the ultimate tensile strength. The refined grain size after RCH treatment results in a flow stress increase of 7%. The changed phases in CGHAZ and ICCGHAZ lead to an increase of the flow stress in comparison with the as received steel, by 44% and by 14%, respectively.

2.3. Fracture toughness tests

Fracture toughness tests were performed [29,30] according to the standard ISO 12135 [32] using sub-sized Single Edge Notched Bending (SENB) specimens, with dimensions of 20 mm × 10 mm × 92 mm. Fig. 6

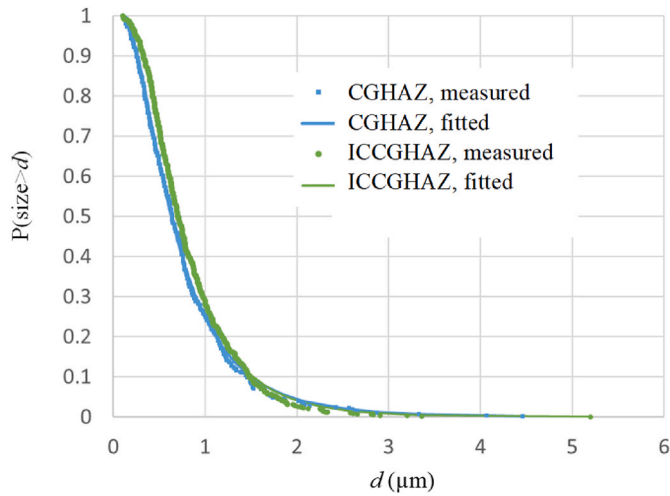


Fig. 4. Distribution of longer axis of M-A constituents in HAZs.

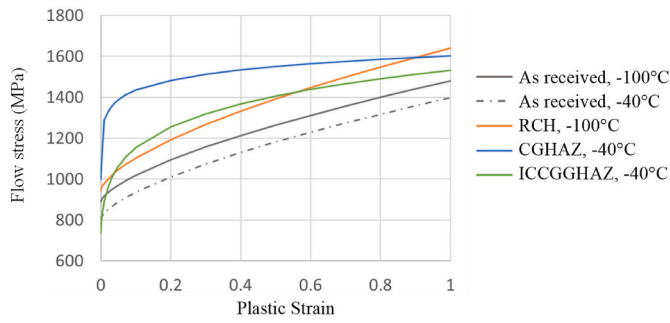


Fig. 5. Flow stress vs plastic strain curves of steels.

Table 2
Summary of tensile test results [29,30].

Material	Temperature °C	Yield strength (MPa)	Tensile strength (MPa)
CGHAZ	-40	1000 (±30)	1470 (±50)
ICCGHAZ	-40	740 (±20)	1240 (±50)
RCH	-100	942 (±24)	1068 (±20)
As received	-40	780 (±5)	930 (±10)
As received	-100	895 (±12)	1013 (±13)

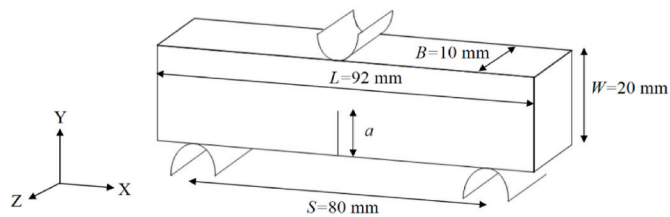


Fig. 6. Geometry layout of the SENB specimen [26].

shows the geometry of the SENB specimens, including crack length a and specimen height W . Fracture tests to study grain refinement were performed on deep cracked ($a/W = 0.5$) specimens, the initial crack length is 10 mm; including a 8.6 mm notch and a 1.4 mm pre-fatigued crack. Fracture tests to study HAZs were performed also on shallow cracked ($a/W = 0.1$) specimens; the initial crack length is 2 mm, including a 1.4 mm notch and a 0.6 mm pre-fatigued crack.

All fracture specimens were tested in 3-point bending at a loading rate of 2 mm/s using a MTS servo hydraulic. Table 3 summarizes the

Table 3
Summary of fracture tests [29,30].

a/W	Material	Number of samples	Test Temperature °C	Measured CTOD (mm)
0.5	As	14	-100	0.012 (±0.004)
	received	9	-40	0.109 (±0.076)
	CGHAZ	10		0.023 (±0.006)
	ICCGHAZ	9		0.071 (±0.019)
	RCH	8	-100	0.074 (±0.054)
0.1	As	13		0.039 (±0.026)
	received			
	CGHAZ	10	-40	0.065 (±0.157)
	ICCGHAZ	9		0.094 (±0.049)

number of samples and test temperatures for each material.

3. Methods

3.1. Finite element model

SENB specimens are modelled in Abaqus 2017 for each type of steel. A quarter of the specimen ($L/2 \times B/2 \times W$) is modelled as 3D deformable solid by using symmetry as shown in Fig. 7 (a). A quarter of the specimen ($L/2 \times B/2 \times W$) is modelled by using symmetry. Analytical rigid surfaces with frictionless contact are used to model the support and load roller. The initial pre-fatigued crack tip is modelled as a finite notch that is 0.005 mm in radius. The mesh near the crack tip is shown by Fig. 7 (b), where 20-noded hexahedral element with reduced integration (C3D20R) is used. The dimension of the smallest element is 0.001 mm \times 0.005 mm \times 0.067 mm. A total deflection of 1 mm is applied by displacement control. The geometric and material nonlinearity is solved by a full Newton-Raphson algorithm in an implicit method.

3.2. Micromechanism-based cleavage model

The model applied in this paper is developed in Ref. [26] and is based on a multiple-barrier cleavage theory [27,28]. The mechanism represents cleavage fracture in steels as the successive occurrence of three microscale events (as illustrated by Fig. 8).

- I nucleation of a slip-induced crack in a brittle second-phase particle or inclusion;
- II propagation of the microcrack of a particle-size length across the particle/matrix interface;
- III propagation of the crack of a grain-size length across the grain boundary.

The stress level in a hard particle needs to exceed the particle strength σ_H^c to allow a micro-crack nucleation (event I). The value of particle strength is assumed to be uniformly distributed in the range $[\sigma_H^c, \sigma_H^c + \Delta\sigma_H^c]$. The number of cracked inclusions (N_{cr}) is proportional to the stress σ_H at the hard particle. For a volume that initially contains N particles, N_{cr} can be calculated if $\sigma_H > \sigma_H^c$ as:

$$N_{cr} = \min\{N \times (\sigma_H - \sigma_H^c) / \Delta\sigma_H^c, N\} \quad (4)$$

where the stress σ_H is calculated from the stress of the matrix (first principal stress $\sigma_{1,m}$ and the equivalent von Mises stress $\sigma_{eq,m}$), by

$$\sigma_H = \sigma_{1,m} + f_a \sigma_{eq,m} \quad (5)$$

where f_a is based on the inclusion geometry and is determined using the analytical expression in Ref. [33].

For the crack propagation events, i.e., across the particle/matrix interface (event II) and across the grain boundary (event III), stress criterion are used. A minimum crack size equal to particle size (d_c) (event II) or rather grain size (D_c) (event III) is calculated for the first

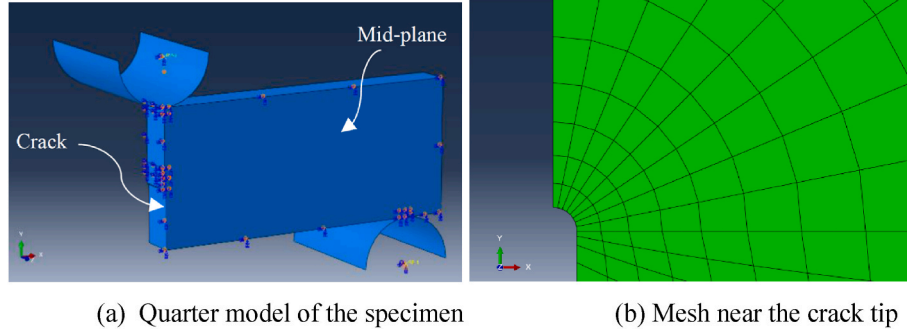


Fig. 7. Finite element model of the three-point bending test.

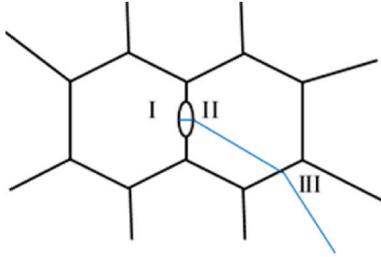


Fig. 8. Critical events of cleavage fracture.

principal stress within the grain ($\sigma_{1,m}$) to propagate the micro-crack, respectively by:

$$d_c = (K_{Ia}^{pm} / \sigma_{1,m})^2 \quad (6)$$

$$D_c = (K_{Ia}^{mm} / \sigma_{1,m})^2 \quad (7)$$

where K_{Ia}^{pm} is the local cleavage parameter to characterize the equivalent toughness at the particle/matrix, and K_{Ia}^{mm} is the local cleavage parameter to characterize the equivalent toughness at the grain boundary.

Fig. 9 gives a flow chart of the computational model to calculate the cleavage probability of macroscale specimens (P_f), which is expressed as

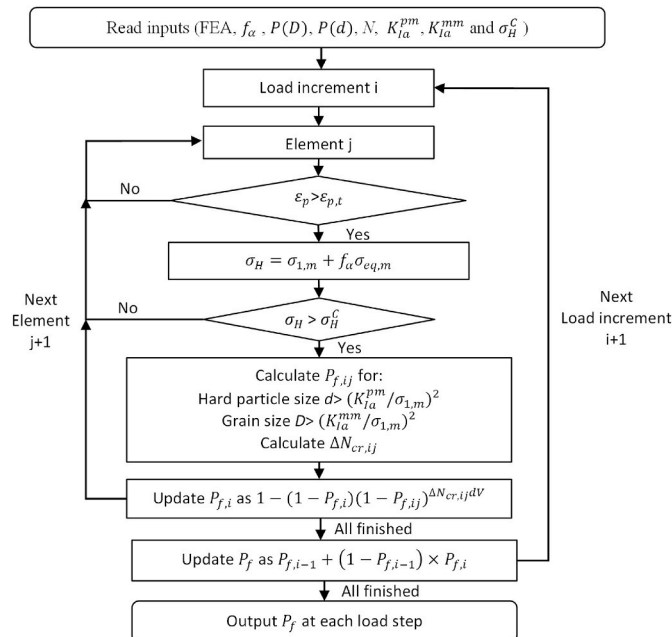


Fig. 9. Flow chart of the computational scheme [26].

a function of the global load. The stress/strain distribution (which contains $\sigma_{1,m}$, $\sigma_{eq,m}$, and ε_p values for each finite element) of a macroscopic specimen is calculated by Finite element analysis (FEA) at each load increment. Based on the stress level, shape of the stress field, and statistical information of the microstructure, the cleavage probability of a finite element is calculated considering the cleavage barriers. The total failure probability of the specimen is calculated as the cleavage probability of all finite elements in the fracture process zone (areas that are plastically deforming). In addition to FEA inputs, other required input includes cleavage parameters (K_{Ia}^{pm} , K_{Ia}^{mm} and σ_H^c) and several microstructural parameters (f_α calculated from inclusion geometry, the distribution function of the grain size $P(D)$, the distribution function of the hard particle size $P(d)$, number of inclusions N per unit of volume). Other predefined parameters are threshold plastic strain $\varepsilon_{p,t}$, elementary volume V_0 , and scatter of the inclusion fracture strength $\Delta\sigma_H^c$. All predefined values are summarized in Table 4. In this article, σ_H^c is determined for each type of inclusion, and $\Delta\sigma_H^c$ represents size effect and variety of local defects in inclusions. The predefined value of $\Delta\sigma_H^c$ is a proxy determined by sensitivity study [26] and is relatively small compared to σ_H^c . The value of $\Delta\sigma_H^c$ and its effect on the simulation results will be more significant when representing scatter among multiple types of inclusions.

4. Results

4.1. Simulation of base material

Analysis of the as-received steel indicates that micro-crack propagation is grain-size controlled [26], as the brittle inclusions have a relatively large dimension (95% of brittle inclusions are larger than 1.5 μm), and the nucleated microcracks are in sizes that enable them to propagate into the surrounding grain. Among the inclusions that are identified as local cleavage fracture initiation sites in Ref. [34], the minimum size is $1.22 \pm 0.08 \mu\text{m}$ (in specimen $a/W = 0.5$) and $1.27 \pm 0.10 \mu\text{m}$ (in specimen $a/W = 0.1$). Such inclusion sizes represent the minimum length of micro-cracks that are able to propagate across the inclusion/matrix interface to form cleavage facets in neighbouring grains. Stress state ($\sigma_{1,m}$) at the crack initiation site was determined by FEA in Ref. [26]. K_{Ia}^{pm} was determined as $2.5 \text{ MPa}\sqrt{\text{m}}$ by eq. (6) with the identified particle size and $\sigma_{1,m}$ [38]. Maximum likelihood fitting is used to determine cleavage parameters K_{Ia}^{mm} and σ_H^c from the measured crack

Table 4
Value of the pre-defined input parameters.

Parameters	Values
Threshold plasticity strain $\varepsilon_{p,thre}$	10^{-5}
Elementary volume V_0	0.001 mm^3
Stress concentration factor of spherical inclusion f_α	0.239
Scatter of the inclusion fracture strength $\Delta\sigma_H^c$	100 MPa

tip opening displacement (CTOD) of high-and low-constraint specimens. The failure probability, P_f of a specimen fractured in experiment, was calculated as a rank probability according to Ref. [35]:

$$P_f = \frac{i - 0.3}{N + 0.4} \quad (8)$$

where i is the rank number in terms of CTOD and N is the total number of experiments.

The fitting on specimens fractured at temperature -100°C is reported in Ref. [26], which results in σ_H^C equals to 2.7 GPa for oxides and 2.2 GPa for rectangular inclusions; K_{Ia}^{mm} equals to 19.5 $\text{MPa}\sqrt{\text{m}}$ for both. From fracture surface analysis in Ref. [26], initiation sites can be identified in nine of the specimens, and seven of them have initiation sites identified as Nb inclusions, which corresponds to the lower σ_H^C . Fitting on specimens fractured at temperature -40°C is performed assuming the same value for σ_H^C , and K_{Ia}^{mm} is determined by inverse analysis on high constraint specimens. The resulting K_{Ia}^{mm} is 22.6 $\text{MPa}\sqrt{\text{m}}$. Fig. 10 shows the comparison of experiments and the simulation using the fitted parameters.

4.2. Simulation of grain size refinement specimens

After RCH, the inclusions are unaltered (same size, composition, shape, and distribution), and σ_H^C is assumed to have the value determined from the reference steel, 2.7 GPa for oxides and 2.2 GPa for rectangular inclusions. Cleavage parameter K_{Ia}^{mm} (grain boundary toughness) is determined by inverse analysis (maximum likelihood fitting) from the measured CTOD of high-constraint specimens. The resulting K_{Ia}^{mm} is 17.6 $\text{MPa}\sqrt{\text{m}}$. Fig. 10 shows the comparison of experiments and the simulation using the fitted parameters.

If the grain refined material is simulated with the K_{Ia}^{mm} value of the as-received steel, rather than with the fitting, the distribution of calculated CTOD is shown by the dashed line in Fig. 11. The assumption of unaltered K_{Ia}^{mm} results in calculated CTOD much higher than the experimental values. With unaltered K_{Ia}^{mm} , the grain refinement corresponds to the measured fracture toughness will be 46%. It is lower than the actual grain refinement by 55%. In another words, the experimental improvement of toughness based on grain size refinement is 80% of what would be expected based on simulations.

4.3. Simulation of HAZ

The oxides and Nb-rich inclusions have been identified to trigger cleavage in the as-received steel [34]. However, clear river lines were not observed on the fracture surface of HAZs [30]. Particles that resemble M-A constituents are present at cleavage facets where river lines appear to be converging, which are likely initiation sites [30]. Thus which type of the particles act as the initiation sites cannot be determined, and it may suggest multiple initiation sites. It is firstly assumed

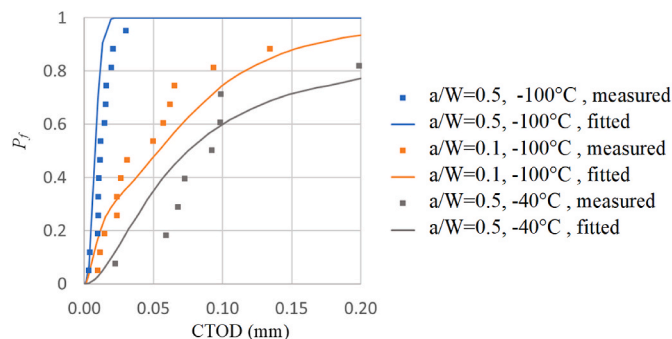


Fig. 10. Cleavage probability calculation of as-received steel.

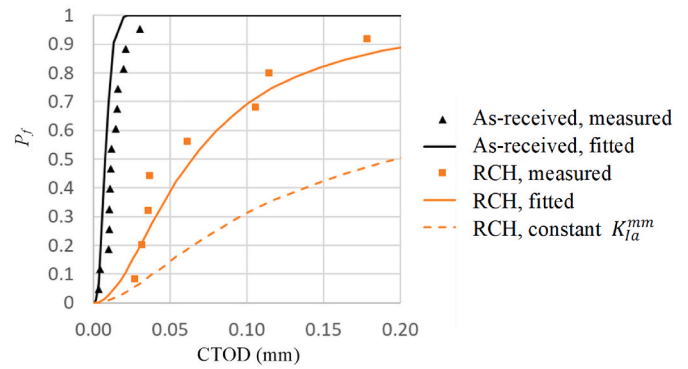


Fig. 11. Cleavage probability calculation of $a/W = 0.5$ specimens fractured at -100°C .

that cleavage is triggered by both inclusions and M-A constituents. The parameters are fitted based on both high- and low-constraint specimens with the following assumed: σ_H^C for M-A and K_{Ia}^{mm} for grain boundaries are fitted, that σ_H^C is assumed to be constant for M-A among CGHAZ and ICCGHAZ, while K_{Ia}^{mm} is assumed to vary. In order to clarify the influence of assumptions of initiation site, simulations with two additional underlying assumptions are performed: (i) only inclusions initiate cleavage, (ii) only M-A constituents initiate cleavage. When inclusions are assumed to trigger the final fracture, the fracture stress σ_H^C for circular and rectangular inclusions are the same as in the base material, and K_{Ia}^{mm} for grain boundaries is fitted for the HAZ material; when M-A constituents are assumed to trigger the final fracture, cleavage parameters σ_H^C for M-A and K_{Ia}^{mm} for grain boundaries are fitted. The fitted cleavage parameters are summarized in Table 5, and the comparison of simulations and experiments are shown in Fig. 12.

4.4. Numerical study on grain size and flow stress

To compare the heat-treated materials' fracture behavior with theoretical calculations, a systematic study on grain size and flow stress is performed by means of numerical simulations. A series of simulations to show the effect of grain size is performed for fracture occurring at -100°C and -40°C with cleavage parameters determined from the as-received material, assuming grain sizes are changed independently from all other modelling parameters. As flow stress can be increased by the refined grain size, another simulation is performed to estimate this influence. Fig. 13 shows the sensitivity of CTOD values to the material factors, where the CTOD and the independent parameters are both normalized by the value of the as-received steel. The calculated CTOD is represented by the median value.

For a heat treated steel, the correlation between grain size and yield strength can be assumed to follow a Hall-Petch relationship:

$$\sigma = \sigma_0 + KD^{-1/2} \quad (9)$$

Therefore, the detrimental effect on toughness caused by increased yield stress is less than the improving effect of refined grain size.

Table 5
Fitted cleavage parameters for HAZ and as received steel at -40°C .

Initiator of micro-crack	σ_H^C of M-A (GPa)	K_{Ia}^{mm} ($\text{MPa}\sqrt{\text{m}}$)			σ_H^C of inclusion (GPa) ^a
		CG	ICCG	As received	
Inclusion	–	38.5	33.4	22.6	2.7 for oxides and 2.2 for rectangular
M-A	2.0	39.4	32.2	–	inclusions (NbC)
M-A & inclusion	2.2	41.1	35.0	–	

^a Fitted from as received steel and is considered as a constant value after heat treatment.

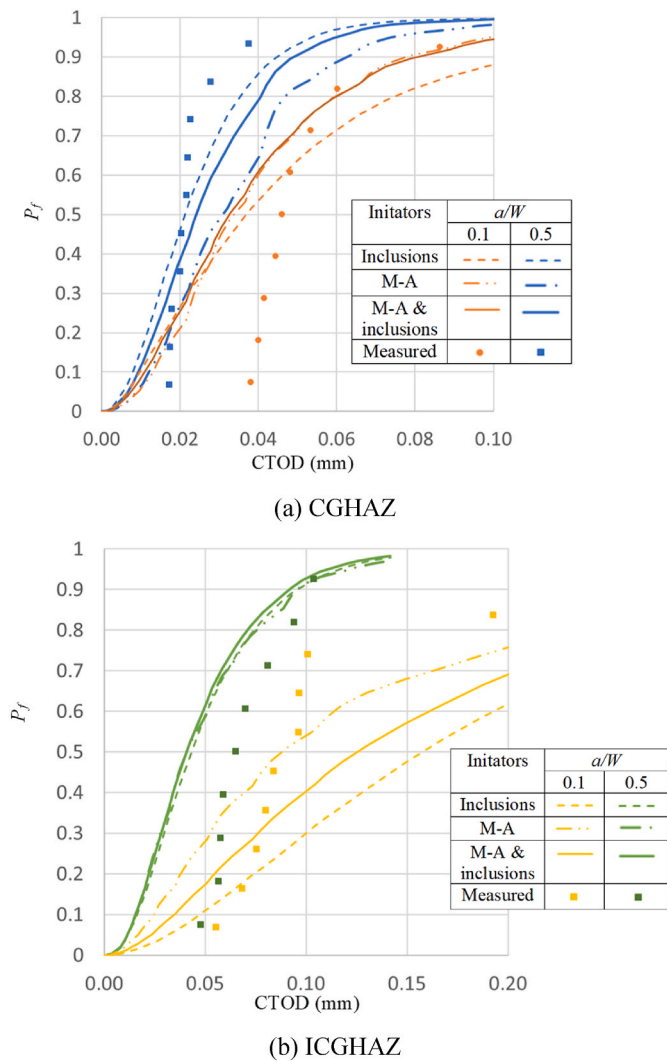


Fig. 12. Cleavage probability calculation of HAZ specimens fractured at $-40\text{ }^{\circ}\text{C}$.

For the as-received material, the power-law part of eq. (1) characterizes the large grains that initiate cleavage crack. Fig. 2 shows that if only the log-normal distribution is used then the number of grains in the large-size tail would be significantly overestimated. However, the grains characterized by the lognormal part can also contribute to the cleavage in a coarse-grain material, for example in the sensitivity study shown by Fig. 13 (a). Using a combined function to represent the grain size distribution is thus essential to accurately capture the relationship between grain size and fracture toughness.

4.5. Numerical study on particle size and density

Reducing the density or refining hard particles that initiate microcracks is another method to improve toughness through microstructure control [4]. However, for the HAZ specimens, it is not determined if M-A or inclusions are the dominant hard particles that initiate the primary cleavage crack. A sensitivity study on particle size and density is performed by means of numerical simulation of the HAZ specimens.

The simulations are performed for ICCGHAZ specimens fractured at $-40\text{ }^{\circ}\text{C}$. The cleavage parameters are determined from the ICCGHAZ with the assumption of both M-A and inclusions initiating the primary cleavage crack. Fig. 14 shows the sensitivity of CTOD values when assuming M-A or inclusions are removed from the material. The results suggest that the simulated CTOD of high constraint specimens is not

sensitive to the presence of M-A, while removing inclusions effectively increase the CTOD values. M-A constituents are more responsible for initiating cracks in low constraint specimens, as the effect of removing M-A to improve the CTOD values is at the same level as of removing inclusions.

Alternative to removing hard particles, refining hard particles can also effectively improve toughness [24]. Fig. 15 shows the changes of simulated CTOD when assuming inclusions sizes are refined. The results show that refining inclusions sizes by 20% can effectively increase the CTOD values of both high and low constraint specimens, and further refining will contribute less. For M-A, the simulated CTOD of high constraint specimen is not sensitive to refining the M-A, while in low-constraint specimens, the effect of refining M-A is at the same level as of refining inclusions.

5. Discussion

In this research, cleavage behaviours of heat treated S690 QT steel at $-100\text{ }^{\circ}\text{C}$ and $-40\text{ }^{\circ}\text{C}$ are modelled. The simulation results are discussed and compared in this section. Table 6 summarizes the changes in key properties of the steels after three different heat treatments.

5.1. Temperature dependence of K_{Ia}^{mm} for as-received steel

It has been shown in Ref. [27] that the cleavage parameter of particle/matrix interface K_{Ia}^{pm} is independent of temperature and the cleavage parameter of grain boundaries K_{Ia}^{mm} is strongly temperature dependent in the ductile-to-brittle transition range. In the present paper, K_{Ia}^{mm} of as-received S690 QT steel is found to increase by 13% when the temperature is raised from $-100\text{ }^{\circ}\text{C}$ to $-40\text{ }^{\circ}\text{C}$. The tendency agrees with reported findings in Ref. [27]. The increasing K_{Ia}^{mm} with temperature also agrees with the observations obtained from acoustic emission measurements in Ref. [28], which suggests that at increasing temperature, cleavage is controlled by the propagation of microcracks arrested at grain boundaries.

The temperature dependence for surface energy γ_{mm} of grain boundaries was measured in Refs. [36,37] from the analysis of initiation facets. Taking the results from Ref. [36] as a reference, the value of γ_{mm} is increased by 46% when the temperature is raised from $-100\text{ }^{\circ}\text{C}$ to $-40\text{ }^{\circ}\text{C}$. Applying the relationship $K_{Ia}^{mm} \propto \sqrt{\gamma_{mm}}$ [36,37], the 46% increase in γ_{mm} results in a 21% increase in K_{Ia}^{mm} . However, it should be noted that the relationship shows large diversity for different types of steel, and the results in Refs. [36,37] are for ferrite-pearlite microstructures.

5.2. The effect of RCH treatment

The objective of the RCH treatment was to reduce the grain size while retaining the phases of the as-received material. After the post-process heat treatment, grain refinement of 57% (in terms of average value) was achieved, with the flow stress increased by 7%. The average CTOD of the heat-treated steel is increased by 516% with respect to the as-received steel. The fitted cleavage parameter K_{Ia}^{mm} is lower than for the as-received steel, which indicates that the grain refinement on toughness improvement is not fully effective as the equivalent resistance to crack propagation decreases.

Grain boundary misorientation angles for the as-received steel and the heat-treated steel are shown in Fig. 16. Low-angle misorientations are typically distributed between laths, while high-angle misorientations, including packet and block boundaries, are distributed within PAG. For the studied steel, the fraction of high misorientation angles ($>15^{\circ}$) remains constant around 90% after heat treatment. The peaks around 60° show a certain decrease after the heat treatment.

The high-angle misorientations are beneficial for the toughness because they are effective barriers and cause cracks to deviate. The lower number fraction of high-angle misorientations (the peak of the

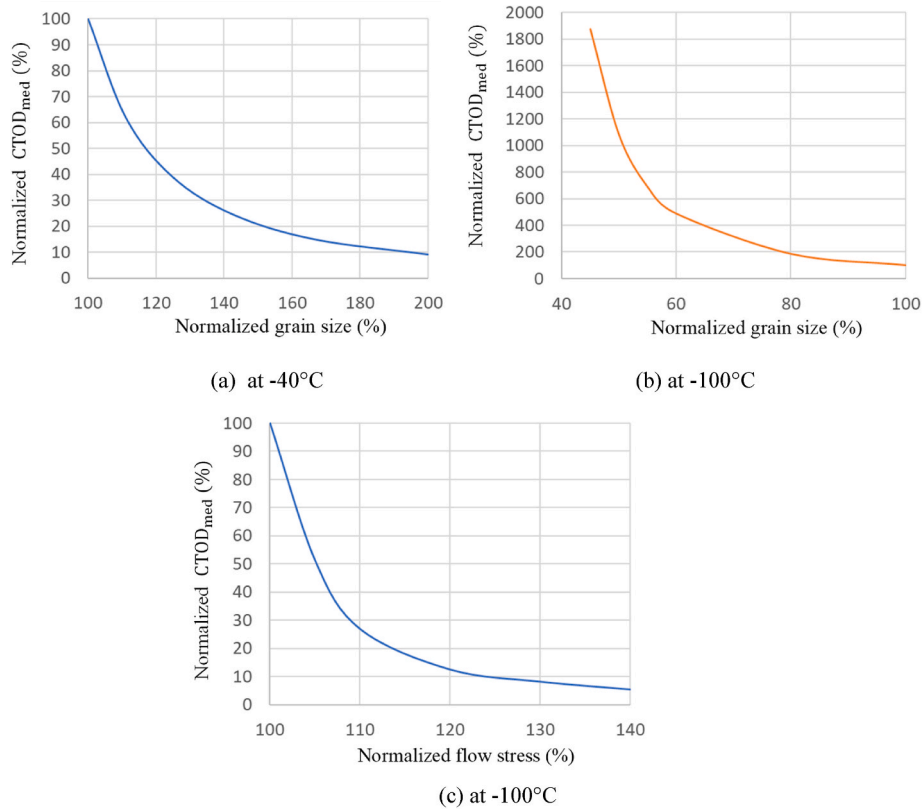


Fig. 13. Simulated median CTOD with (a) increased grain size (b) decreased grain size and (c) flow stress (CTOD values and the independent parameters are normalized by the value of as-received steel).

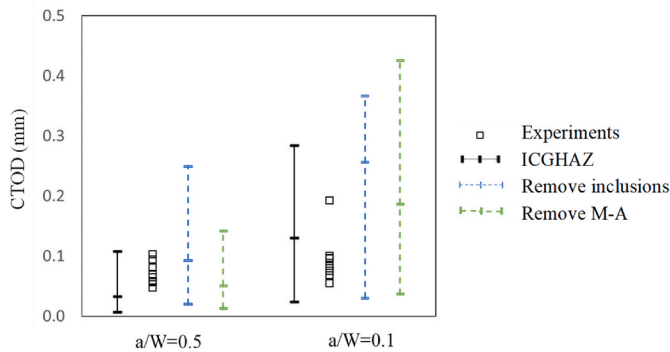


Fig. 14. Changes of simulated CTOD when assuming hard particles are removed (lines correspond to Min-Median-Max in simulated CTOD values).

distribution, which is in 55–60°) reduces the efficiency of refined grain size on toughness improvement. In Ref. [29], the packet size and block widths for the as-received and the grain-refined S690QT steel are presented. The average packet size and block width were reduced around 60% and 40%, respectively. The block width reduction is lower than the refinement of PAG size, which explains the lower number fraction of misorientation angles around 60° after RCH.

5.3. Effect of CGHAZ and ICCGHAZ

After the heat treatment, grains are coarsened by 195% and 237% (in terms of average value), for CGHAZ and ICCGHAZ respectively. The phase fractions are also changed, which leads to an increase of the flow stress. The flow stress is increased by 44% for CGHAZ and by 14% for ICCGHAZ. The average CTOD of CGHAZ is 80% lower and the average

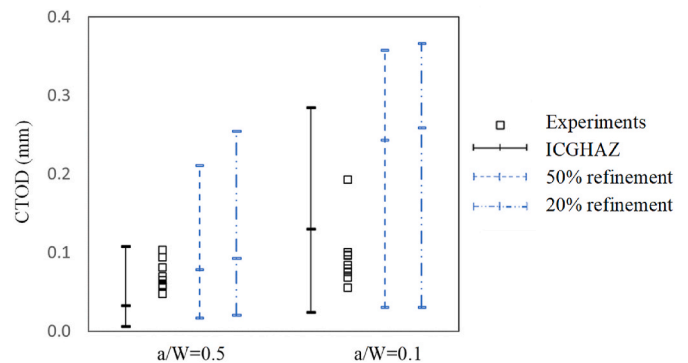


Fig. 15. Changes of simulated CTOD when assuming inclusions are refined (lines corresponds to Min-Median-Max in simulated CTOD values).

Table 6

Changes of properties relative to as-received steel.

Heat treatment	Flow stress	Grain size	CTOD
RHC	↑7%	↓57%	↑516%
CGHAZ	↑44%	↑195%	↓80%
ICCGHAZ	↑14%	↑237%	↓35%

CTOD of ICCGHAZ is 35% lower than for the as-received steel. However, the detrimental effect of the coarse grains and high flow stress is not as pronounced as expected, if compared with sensitivity study shown in Figs. 12 and 13. When fitting the cleavage parameter K_{Ia}^{mm} , the effect is reflected by a very high value of K_{Ia}^{mm} for the HAZ, which represents more effective resistance to micro-crack propagation compared with the as-received steel.

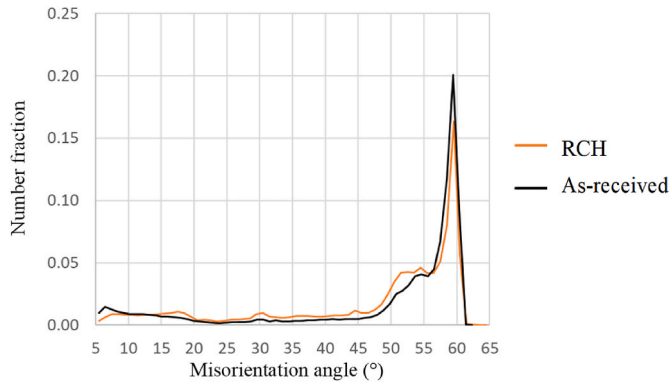


Fig. 16. Grain boundary misorientation angle of as-received steel and steel after RCH [29].

This finding cannot be explained by the differences in the lath/block/packet structures within PAGs. Grain boundary misorientation angles for the as-received material and the HAZ are shown in Fig. 17, which have no significant difference. In Ref. [30], M-A constituents are found along the propagation path of secondary cracks by EBSD analysis, and some M-A constituents are observed to deflect the crack. Kernel Average Misorientation (KAM) maps have been measured for the HAZ in Ref. [30]. According to the KAM maps, the M-A constituents are the areas with the largest KAM values, indicating a large strain located in M-A constituents. It is a consequence of the residual stresses induced during phase transformation to martensite and the retention of austenite during cooling. The residual stress is compressive in M-A constituents and is tension in the matrix surrounding the M-A constituents [22]. When a crack interacts with M-A constituents, the compressive stresses within M-A constituents can reduce the stress intensity, which explains the crack arrest events in HAZ.

The residual stress in M-A constituents may also have effects on the initiation stage and the propagation of micro-cracks across particle/matrix interface. For example, the residual stress in matrix around the M-A is tension and leads to lower K_{Ia}^{pm} , while the compressive residual stress in M-A leads to higher σ_H^C . The assumption of constant K_{Ia}^{pm} and σ_H^C , which is used in the modelling of HAZ materials, may be violated if the residual stresses are different between CGHAZ and ICCGHAZ. It can be observed that the quality of fittings of simulated HAZs (Fig. 12) are in general worse than the fittings of as received (Fig. 10) and RCH steel (Fig. 11). Not considering the effect of residual stress is a possible cause for the poorer match between experimental and simulation results of HAZ materials. However, simply shifting σ_H^C in eq. (4) by a fixed quantity corresponding to the estimated residual stresses did not improve the model performance. As the residual stresses are related to plastic deformation, the effect cannot be modelled by superposition. Instead, a

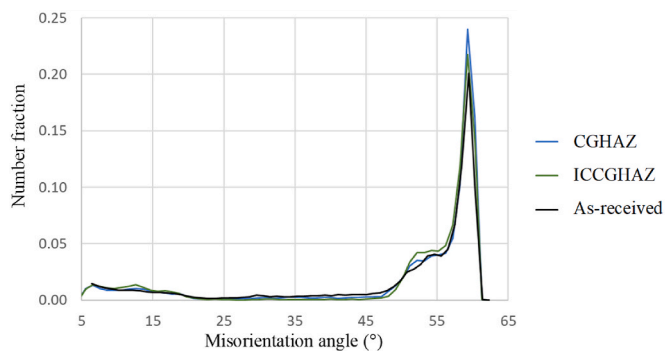


Fig. 17. Grain boundary misorientation angle of HAZ compared to as-received steel [30].

threshold value of the CTOD is observed for CGHAZ and ICCGHAZ, which suggests that a threshold plastic strain value may be required for HAZ materials.

6. Conclusions

In this research, a microstructure-based method that is coupled with Finite Element Analysis is used to model the cleavage behavior of heat treated S690 QT steel at $-100\text{ }^{\circ}\text{C}$ and $-40\text{ }^{\circ}\text{C}$. Cleavage simulations of steel after rapid cyclic heating and heat affect zones are performed. By simulating cleavage fracture of various microstructures and comparing with experiments, the effect of different types of microstructures on cleavage is quantitatively estimated. The following conclusions are highlighted.

- The fitted cleavage parameter K_{Ia}^{mm} decreases 10% after RCH. The experimental improvement of toughness based on grain size is 80% of what would be expected based on multi-barrier simulations. After RCH, the block width reduction is lower than the refinement of PAG size, which is the reason for the lower number fraction of high-angle misorientation boundaries and less effective improvement on fracture toughness.
- The fitted cleavage parameter K_{Ia}^{mm} of HAZs is more than 40% higher than of the as-received steel, which represents effective resistance to micro-crack propagation. The fitted K_{Ia}^{mm} of ICCGHAZ is 13–18% lower than the value of CGHAZ. The more pronounced crack arrest events in HAZ are likely to be explained by the reduction of crack tip stresses due to the interaction with residual compressive stresses in M-A.
- It is not determined if M-A or inclusions are the dominant hard particles that initiate the primary cleavage cracks for the HAZ specimens. While assuming that M-A initiates the microcracks slightly improves the fitting to shallow-cracked specimens of ICCGHAZ, numerical simulations show that reducing or refining inclusions more effectively improves fracture toughness than reduction or refining M-A.

The effectiveness of grain refinement through a simple heat treatment route to improve cleavage fracture is assessed. It reveals how model parameters should be adjusted to account for changes in prior austenite grain sub-structures, which may assist in the fracture behavior prediction for the improvement of design for high strength steels. The degradations of toughness in CGHAZ and ICCGHAZ are studied considering the changes in grain structure, brittle particles, and yield properties, through both experimental and modelling approaches. It shows that the influence of M-A constituents in HAZs on crack propagation should be studied.

The HAZ specimens in the current paper are produced with Gleeble heat treatment and are considered as homogenous in the model. The work here will enable future work in which macroscopically heterogeneous weld zone are modelled. When the method is applied on an actual weld, the gradient of microstructure and stress should be included. In addition, the current method has the following limitations that should be investigated further.

- This paper only studies pure cleavage; the interaction with ductile fracture is not considered.
- The cleavage parameter K_{Ia}^{mm} used in the current model is found to be temperature dependent. The micromechanism to explain this temperature dependence can be further explored.
- The current model does not directly account for the morphology of M-A constituents and residual stress distributions in/around them.

CRedit authorship contribution statement

Quanxin Jiang: Writing – original draft, Writing – review & editing, Visualization, Validation, Methodology, Investigation, Formal analysis, Data curation, Conceptualization. **Virginia M. Bertolo:** Writing – review & editing, Validation, Methodology, Investigation, Data curation, Conceptualization. **Vera Popovich:** Writing – review & editing, Validation, Supervision, Methodology, Conceptualization. **Jilt Sietsma:** Writing – review & editing, Supervision, Methodology, Conceptualization. **Carey L. Walters:** Writing – review & editing, Supervision, Methodology, Conceptualization.

Declaration of competing interest

The authors declare that they have no known competing financial interests or personal relationships that could have appeared to influence the work reported in this paper.

Data availability

Data will be made available on request.

Acknowledgement

The authors acknowledge the support in the Micro-Tough research project (n. 16350) from the Dutch Research Council (NWO) and the consortium of partners that include Allseas Engineering, Dillinger, Lloyd's Register, The Dutch Ministry of Defence, and TNO.

References

- [1] EN 1011, CEN, Welding – Recommendations for Welding of Metallic Materials, 2009.
- [2] T. Miyata, R.C. Yang, A. Otsuka, T. Haze, S. Ahira, Cleavage fracture of steels with fine grained ferrite, coarse grained bainitic and martensitic, in: *Advances in Fracture Research Proceeding of the Seventh International Conference of Fracture*, 1989, pp. 2563–2571.
- [3] S. Lee, S. Kim, B. Hwang, B.S. Lee, C.G. Lee, Effect of carbide distribution on the fracture toughness in the transition temperature region of an SA 508 steel, *Acta Mater.* 50 (19) (2002) 4755–4762.
- [4] M.W. Zhou, H. Yu, Effects of precipitates and inclusions on the fracture toughness of hot rolling X70 pipeline steel plates, *Int. J. Miner. Metall. Mater.* 19 (9) (2012) 805–811.
- [5] X. Li, X. Ma, S.V. Subramanian, C. Shang, R.D.K. Misra, Influence of prior austenite grain size on martensite-austenite constituent and toughness in the heat affected zone of 700MPa high strength linepipe steel, *Mater. Sci. Eng.* 616 (2014) 141–147.
- [6] P. Trampus, Micro structural aspects of unstable crack propagation in ferritic steels, *Mater. Sci. Forum* 537–538 (2007) 465–472.
- [7] S. Morito, H. Saito, T. Ogawa, T. Furuhashi, T. Maki, Effect of austenite grain size on the morphology and crystallography of lath martensite in low carbon steels, *ISIJ Int.* 45 (2005) 91–94.
- [8] J.W. Morris, Z. Guo, C.R. Krenn, Y.H. Kim, The limits of strength and toughness in steel, *ISIJ Int.* 41 (2001) 599–611.
- [9] R.L. Miller, Ultrafine-grained microstructures and mechanical properties of alloy steels, *Metall. Mater. Trans.* 3 (1972) 905–912.
- [10] H.J. Kim, Y.H. Kim, J.W. Morris, Thermal mechanisms of grain and packet refinement in a lath martensitic steel, *ISIJ Int.* 38 (1998) 1277–1285.
- [11] R. Song, D. Ponge, D. Raabe, Mechanical properties of an ultrafine grained C-Mn steel processed by warm deformation and annealing, *Acta Mater.* 53 (2005) 4881–4892.
- [12] M.H. Park, A. Shibata, N. Tsuboi, Challenging ultra grain refinement of ferrite in low-C steel only by heat treatment, *Front. Mater.* 7 (2020) 1–10.
- [13] X. Li, J. Zhao, L. Dong, et al., The significance of coherent transformation on grain refinement and consequent enhancement in toughness, *Materials* 13 (2020) 1–15.
- [14] B. Smoljan, An analysis of combined cyclic heat treatment performance, *J. Mater. Process. Technol.* 155–156 (2004) 1704–1707.
- [15] S. Morito, H. Tanaka, R. Konishi, T. Furuhashi, T. Maki, The morphology and crystallography of lath martensite in Fe-C alloys, *Acta Mater.* 51 (2003) 1789–1799.
- [16] D. Liu, M. Luo, B. Cheng, R. Cao, J. Chen, Microstructural evolution and ductile-to-brittle transition in a low-carbon MnCrMoNiCu heavy plate steel, *Met. Mater. Trans. A* 49 (2018) 4918–4936.
- [17] K. Shibamura, Y. Nemoto, T. Hiraide, K. Suzuki, S. Sadamatsu, Y. Adachi, S. Aihara, A strategy to predict the fracture toughness of steels with a banded ferrite-pearlite structure based on the micromechanics of brittle fracture initiation, *Acta Mater.* 144 (2018) 386–399.
- [18] R. Rodríguez-Martín, I. Ocaña-Arizcorreta, A. Martín-Meizoso, Modelling cleavage fracture in high strength steels and their welds, *Mater. Sci. Forum* 482 (2005) 171–174.
- [19] Q.M. Jiang, X.Q. Zhang, L.Q. Chen, Weldability of 1000 MPa grade ultra-low carbon bainitic steel, *J. Iron Steel Res. Int.* 23 (2016) 705–710.
- [20] S. Lee, B.C. Kim, D.Y. Lee, Fracture mechanism in coarse grained HAZ of HSLA steel welds, *Scripta Metall.* 23 (1989) 995–1000.
- [21] P. Mohseni, J.K. Solberg, M. Karlsen, et al., Investigation of mechanism of cleavage fracture initiation in intercritically coarse grained heat affected zone of HSLA steel, *Mater. Sci. Technol.* 28 (2012) 1261–1268.
- [22] C.L. Davis, J.E. King, Cleavage initiation in the intercritically reheated coarse-grained heat-affected zone, Part I. Fractographic evidence, *Metall. Mater. Trans. A* 25A (1994) 563–573.
- [23] S.G. Lee, B. Kim, S.S. Sohn, et al., Effects of local-brittle-zone (LBZ) microstructures on crack initiation and propagation in three Mo-added high-strength low-alloy (HSLA) steels, *Mater. Sci. Eng., A* 760 (2019) 125–133.
- [24] Y. Li, T.N. Baker, Effect of morphology of martensite-austenite phase on fracture of weld heat affected zone in vanadium and niobium microalloyed steels, *Mater. Sci. Technol.* 26 (2010) 1029–1040.
- [25] M.G. Vassilaros, Fracture Behavior of Ultra-low-carbon Steel Plate and Heat-Affected Zone, DTIC report, 1990, ADA235638.
- [26] Q. Jiang, V.M. Bertolo, V.A. Popovich, J. Sietsma, C.L. Walters, Microstructure-informed statistical modelling of cleavage fracture in high strength steels considering through-thickness inhomogeneities, *Eng. Fract. Mech.* 267 (2022), 108432.
- [27] A. Martín-Meizoso, I. Ocaña-Arizcorreta, J. Gil-Sevillano, M. Fuentes-Pérez, Modelling cleavage fracture of bainitic steels, *Acta Metall. Mater.* 42 (6) (1994) 2057–2068.
- [28] A. Lambert-Perlade, A.F. Gourgues, J. Besson, T. Sturel, A. Pineau, Mechanisms and modeling of cleavage fracture in simulated heat-affected zone microstructures of a high-strength low alloy steel, *Metall. Mater. Trans. A* 35 (13) (2004) 1039–1053.
- [29] V.M. Bertolo, L. Vilasi, Q. Jiang, C.L. Walters, J. Sietsma, V.A. Popovich, Rapid cyclic heating effects on grain refinement, microstructure and cleavage fracture toughness of a S690 high strength steel, *J. Mater. Res. Technol.* 23 (2023) 1919–1933.
- [30] V.M. Bertolo, Q. Jiang, M. Terol Sanchez, A.C. Riemsag, C.L. Walters, J. Sietsma, V.A. Popovich, Cleavage fracture micromechanisms in simulated heat affected zones of S690 high strength steels, *Mater. Sci. Eng. A* 868 (2023), 144762.
- [31] R.T. De Hoff, The determination of the size distribution of ellipsoidal particles from measurements made on random plane sections, *Trans TMS-AIME* 224 (1962) 474–486.
- [32] ISO 12135, Metallic Materials - Unified Method of Test for the Determination of Quasistatic Fracture Toughness, 2018.
- [33] Q. Jiang, V.M. Bertolo, V.A. Popovich, J. Sietsma, C.L. Walters, Relating local stress on a hard microstructural inclusion from far-field stress on matrix to understand cleavage fracture in high strength steel, *Int. J. Fract.* 232 (2021) 1–21.
- [34] V.M. Bertolo, Q. Jiang, S. Scholl, R. Petrov, U. Hangen, C.L. Walters, J. Sietsma, V.A. Popovich, A comprehensive characterisation and quantification of the multiphase microstructure of a thick-section high strength steel, *J. Mater. Sci.* 57 (2022) 7101–7126.
- [35] K. Wallin, Master Curve Analysis of Ductile to Brittle Transition Region Fracture Toughness Round Robin Data: the "EURO" Fracture Toughness Curve, VTT Technical Research Centre of Finland. VTT Publications No, 1998, p. 367.
- [36] I. Kawata, H. Nakai, S. Aihara, Experimental evaluation of effective surface energy for cleavage microcrack propagation across grain boundary in steels, *Acta Mater.* 150 (2018) 40–52.
- [37] J.I.S. Martin, Determination of energetic parameters controlling cleavage fracture in a Ti-V microalloyed ferrite-pearlite steel, *Acta Metall.* 40 (4) (1999) 459–464.
- [38] Q. Jiang, V.M. Bertolo, S. Pallasपुरu, V.A. Popovich, J. Sietsma, C. Walters, Microstructure-based cleavage parameters in bainitic, martensitic, and ferritic steels, *Eng. Fract. Mech.* 281 (2023), 109146.